Compositional landscape for glass formation in metal alloys

Jong Hyun Na[a], Marios D. Demetriou[a,b], Michael Floyd[a], Andrew Hoff[b], Glenn R. Garrett[a], and William L. Johnson[a,b,1]

[a]Glassimetal Technology Inc., Pasadena, CA 91107; and [b]Keck Laboratory, California Institute of Technology, Pasadena, CA 91125

Contributed by William L. Johnson, May 13, 2014 (sent for review March 7, 2014)

A high-resolution compositional map of glass-forming ability (GFA) in the Ni–Cr–Nb–P–B system is experimentally determined along various compositional planes. GFA is shown to be a piecewise continuous function formed by intersecting compositional subsurfaces, each associated with a nucleation pathway for a specific crystalline phase. Within each subsurface, GFA varies exponentially with composition, wheres exponential cusps in GFA are observed when crossing from one crystallization pathway to another. The overall GFA is shown to peak at multiple exponential hypercusps that are interconnected by ridges. At these compositions, quenching from the high-temperature melt yields glassy rods with diameters exceeding 1 cm, whereas for compositions far from these cusps the critical rod diameter drops precipitously and levels off to 1 to 2 mm. The compositional landscape of GFA is shown to arise primarily from an interplay between the thermodynamics and kinetics of crystal nucleation, or more precisely, from a competition between driving force for crystallization and liquid fragility.

metallic glass | amorphous alloy | viscosity | glass transition

The glass-forming ability, or GFA, of a liquid metal alloy is not an intrinsic material attribute, but rather defined by the absence of a viable crystallization pathway as the liquid is undercooled below its thermodynamic melting temperature (1, 2). Crystallization is typically triggered by nucleation of a particular crystalline phase, followed by other competing phases, often catalyzed by the presence of the first phase. Crystal nucleation rates depend not only on temperature, pressure, and alloy composition, but also on extrinsic factors such as the presence of chemical impurities, trace crystalline debris (e.g., oxide inclusions), container wall effects, or shear flow conditions in the liquid, to name a few (3–7). Variations in these extrinsic factors often lead to inconsistent and nonreproducible GFA.

The classical nucleation theory of crystals in undercooled liquids was originally developed by Turnbull (1) to account for the substantial undercooling observed in elemental liquid metals. He later extended his theory to explain metallic glass formation in rapidly cooled low melting eutectic Au–Si and Au–Ge–Si alloys (8, 9). Below the liquidus temperature T_L, the liquid viscosity, $\eta(T)$, rises steeply with falling temperature. A liquid ultimately freezes at a glass transition temperature T_g, where the viscosity reaches a solid-like value of $\sim 10^{12}$ Pa·s. Turnbull considered the "reduced glass transition temperature" $t_{rg} = T_g/T_L$ as a characteristic material parameter. He argued that crystal nucleation rates should fall precipitously as t_{rg} increases, becoming immeasurably small for $t_{rg} \approx 2/3$. This is widely referred to as Turnbull's criteria for bulk glass formation; it has been proven to be a valuable, albeit rough, guide in the development of bulk metallic glasses (10–12).

In the present work, a systematic experimental approach is developed to quantify the intrinsic dependence of GFA on composition for near-eutectic multicomponent metal alloys. The optimization of GFA for quinary Ni–Cr–Nb–P–B alloys is presented as a case study wherein bulk glasses of centimeter thickness are achieved. This quinary system is based on the low melting binary $Ni_{81}P_{19}$ eutectic alloy with small additions of Cr and Nb as substitutes for Ni, and B as a substitute for P.

Binary Ni–P and ternary Ni–Cr–P alloys have long been known to form glassy ribbons of 20 to 40-μm thickness on quenching from the melt at cooling rates of 10^5 to 10^6 K/s using rapid melt quenching approaches such as planar flow casting (13, 14). Following the discovery of bulk metallic glasses, Hashimoto and coworkers (15) as well as Inoue and coworkers (16) investigated bulk glass formation in quinary Ni–Cr–Nb–P–B alloys and identified specific alloy compositions capable of forming metallic glass rods with diameters of 1 to 2 mm. In the current investigation, by using an efficient and reproducible GFA assessment and optimization strategy, we report that maximum attainable metallic glass rod diameters in the same Ni–Cr–Nb–P–B system are an order of magnitude larger (1–2 cm) than reported in prior work.

To accurately quantify the intrinsic composition dependence of GFA requires (*i*) precisely controlling alloy composition and impurity content, (*ii*) quantitatively and reproducibly determining GFA at a specific composition by controlling the sample cooling history, and (*iii*) minimizing the influence of extrinsic factors such as heterogeneous nucleation sites (foreign oxide inclusions, the container wall, etc.) and melt flow conditions during cooling. In this work, alloys with precisely controlled composition were produced from high-purity starting elements. GFA was determined by melting the alloys in silica tubes and subsequently water quenching to form metallic glass rods. The silica tubes exhibit no detectable reaction with the present alloys. Moreover, being a glass, the silica tube is not expected to induce heterogeneous nucleation at the inner wall. Finally, the melt being confined inside the tube during quenching does not undergo significant shear flow. As such, the cooling history of the sample is governed almost solely by conduction without any significant convection, and is therefore expected to be reproducible. GFA is characterized by a critical rod diameter, d_{cr}, defined as the largest diameter rod that can be quenched into a fully glassy structure without detectable crystallinity, as verified by X-ray diffraction. Additional details on the alloy preparation,

Significance

This paper reports and explains the exponential dependence of crystal nucleation rates on alloy composition for an undercooled liquid. It is shown that maxima in alloy glass-forming ability (GFA) take the form of exponential hypercusps in composition space. The approach is illustrated by optimizing the composition of a five-component nickel–chromium-base metallic glass to achieve order-of-magnitude improvements in GFA over prior work. Variations in GFA are shown to arise from the interplay between alloy-melting behavior and the liquid rheology.

Author contributions: J.H.N., M.D.D., and W.L.J. designed research; J.H.N., M.F., A.H., and G.R.G. performed research; J.H.N., M.D.D., A.H., G.R.G., and W.L.J. analyzed data; and J.H.N., M.D.D., and W.L.J. wrote the paper.

The authors declare no conflict of interest.

[1]To whom correspondence should be addressed. E-mail: wlj@caltech.edu.

This article contains supporting information online at www.pnas.org/lookup/suppl/doi:10.1073/pnas.1407780111/-/DCSupplemental.

cooling history, and determination of GFA are presented in *Materials and Methods*.

The quinary Ni–Cr–Nb–P–B system has a 4D composition space with independent variables, w, x, y, and z, where composition is expressed as $Ni_{100-w-x-y-z}Cr_wNb_xP_yB_z$. The variables are in atomic percentages. In Fig. 1*A*, we present a detailed 2D GFA contour map associated with composition variation along 2 degrees of freedom, w and x, while keeping y and z constant at 16.5 and 3, respectively. This high-resolution contour map is based on the measured d_{cr} for 42 alloys. Two distinct local maxima with $d_{cr} \geq 10$ mm are clearly evident in the contour map. More specifically, along the compositional line $x = 4.0625 - 0.125w$ (where y and z are held constant at 16.5 and 3), a ridge interconnecting the two peaks is observed in the GFA landscape. The compositional dependence of GFA along this compositional line is presented in Fig. 1*B*. Along this ridge and within $4.5 < w < 10.5$ (which corresponds to $2.75 < x < 3.5$), d_{cr} is found to vary between 8 and 10 mm, whereas a precipitous dip in the GFA is observed for $w < 4.5$ and $w > 10.5$. At $w = 5.6$ and 8.5 (corresponding to $x = 3.4$ and 3), the compositions $Ni_{71.5}Cr_{5.6}Nb_{3.4}P_{16.5}B_3$ and $Ni_{69}Cr_{8.5}Nb_3P_{16.5}B_3$ are seen to exhibit local maxima with $d_{cr} \geq 10$ mm.

In Fig. 2*A* we present a second 2D GFA contour map associated with composition variation in the x–z plane. This map was generated from GFA data on 58 separate alloy compositions. Another ridge in the GFA landscape is identified in this compositional plane along the compositional line $x = z$ where the sum of transition metals $(w + x)$ and metalloids $(y + z)$ are held constant at 11.5 and 19.5, respectively. The GFA compositional dependence along this line is presented in Fig. 2*B*. Along this ridge with $3 < (x, z) < 4$, d_{cr} varies between 9 and 10 mm, whereas it gradually degrades outside this range. A ridge in GFA along $x = z$ suggests that the GFA dependence on Nb and B contents is strongly correlated. This suggests Nb and B atoms tend to occupy associated sites in the short-range configurational order of the glass structure. It is also worth noting that another shallower peak is identified in this 2D plane, isolated from the $x = z$ ridge near $x = 2$ and $z = 5$, where $d_{cr} \approx 7$ mm.

None of the local maxima identified in the compositional planes of Figs. 1 and 2 necessarily represent a global maximum for the overall GFA. Other higher maxima, including an absolute global maximum, may exist in the 4D composition space along different planes; however such maxima are not expected to be far from the common peaks appearing in the planes of Figs. 1*A* and

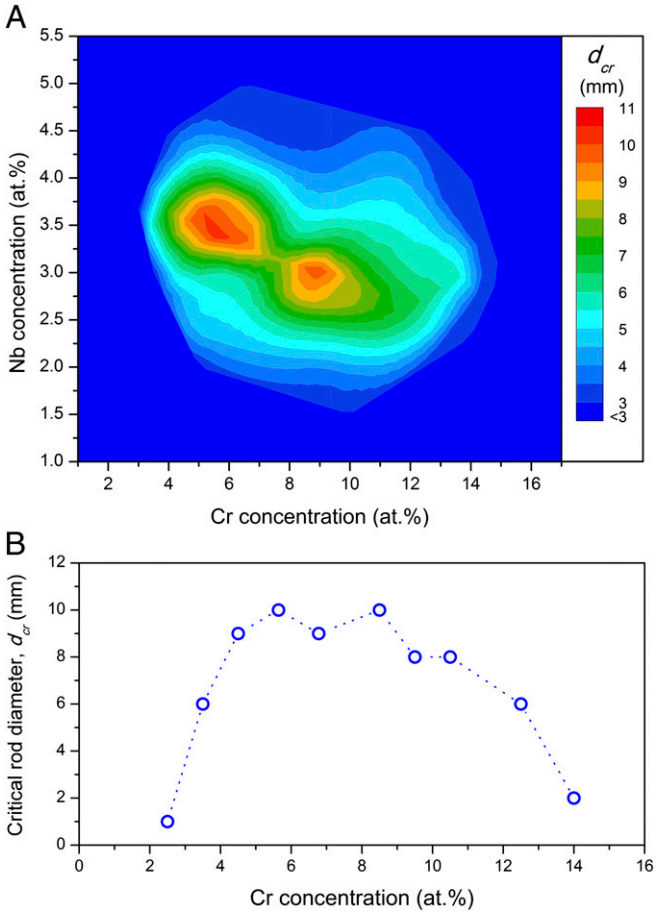

Fig. 1. (*A*) Two-dimensional GFA contour map for $Ni_{80.5-w-x}Cr_wNb_xP_{16.5}B_3$ alloys plotting the critical rod diameter d_{cr} against the Cr and Nb atomic concentrations w and x, while keeping the P and B atomic concentrations y and z constant at 16.5% and 3%, respectively. (*B*) One-dimensional GFA plot for $Ni_{77.4375-0.875w}Cr_wNb_{4.0625-0.125w}P_{16.5}B_3$ alloys plotting the critical rod diameter d_{cr} against the Cr atomic concentration w along the compositional line $x = 4.0625 - 0.125w$ associated with the GFA ridge in the w–x domain shown in *A*. The dotted line is a trend line through the experimental data (open circles).

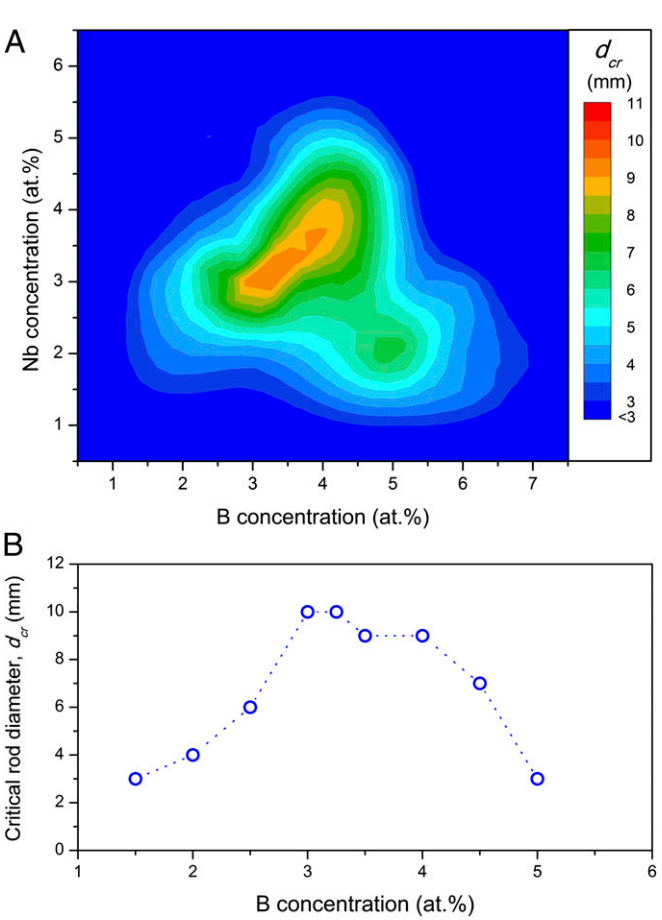

Fig. 2. (*A*) Two-dimensional GFA contour map for $Ni_{69}Cr_{11.5-x}Nb_xP_{19.5-z}B_z$ alloys plotting the critical rod diameter d_{cr} against the Nb and B atomic concentrations x and z, while keeping the sum of Cr and Nb and the sum of P and B atomic concentrations $(w + x)$ and $(y + z)$ constant at 11.5% and 19.5%, respectively. (*B*) One-dimensional GFA plot for $Ni_{69}Cr_{11.5-z}Nb_zP_{19.5-z}B_z$ alloys plotting the critical rod diameter d_{cr} against the B atomic concentration z along the compositional line $x = z$ associated with the GFA ridge in the x–z domain shown in *A*. The dotted line is a trend line through the experimental data (open circles).

2*A*. If a global GFA maximum exists in the current compositional neighborhood it would be hard to predict it given the steepness of the GFA composition maps. In the present work, alloys with an even higher GFA have in fact been discovered for compositions in the neighborhood surrounding $Ni_{69}Cr_{8.5}Nb_3P_{16.5}B_3$. For example, a six-component alloy $Ni_{68.6}Cr_{8.7}Nb_3P_{16}B_{3.2}Si_{0.5}$, which includes a minority addition of Si in its metalloid moiety, demonstrates $d_{cr} \approx 20$ mm when processed by a high-temperature fluxing process (*Materials and Methods*). A fully amorphous 17-mm-diameter rod of $Ni_{68.6}Cr_{8.7}Nb_3P_{16}B_{3.2}Si_{0.5}$, along with an X-ray diffraction pattern and a calorimetric scan verifying its amorphous structure, are shown in Fig. 3.

To map the detailed compositional dependence of GFA in the neighborhood of a peak, we evaluated the GFA along a family of straight lines in the composition space that intersect the peak, where each line is referred to as an "alloy series." The detailed compositional dependence of GFA for four alloy series (labeled I–IV) intersecting the common composition $Ni_{69}Cr_{8.5}Nb_3P_{16.5}B_3$ is presented in Fig. 4. Series I–IV respectively correspond to varying w, x, z, and $(y + z)$ around the composition $Ni_{69}Cr_{8.5}Nb_3P_{16.5}B_3$, which corresponds to a local maximum in GFA in the 4D compositional space. For series I–IV one observes a steeply rising GFA followed by a rapidly decaying GFA as the peak at d_{cr} is traversed. These GFA functions along the composition lines generally consist of piecewise continuous curves, or branches. The curves meet at cusps. It was observed that the individual branches of the GFA map have a roughly exponential dependence on composition (see *SI Materials and Methods* for a list of the exponential fitting parameters.). We argue below that the atomic rearrangement and formation of a critical nucleus within a liquid are both thermally activated processes with associated barrier heights that should depend linearly, to leading order, on composition. As such, an exponential dependence of GFA on composition ensues.

From transition state theory, the nucleation of a phase α (α refers to one of the competing crystalline phases) is expected to be an activated process involving the crossing of a temperature and composition dependent nucleation barrier, $\Delta G_\alpha(T, \mathbf{c})$ (5, 6, 8, 9). The rate at which atomic configurations are sampled in an undercooled liquid is taken to be proportional to the liquid fluidity, or inverse viscosity η^{-1}. Viscous flow is taken to be an activated process that may be characterized by a temperature and composition dependent barrier, $W(T, \mathbf{c})$ (17, 18). The characteristic time for the nucleation of an α-crystal takes the general form

$$\tau_\alpha = \nu^{-1} \exp[\{W(T, \mathbf{c}) + \Delta G_\alpha(T, \mathbf{c})\}/kT], \qquad [1]$$

where ν is an attempt frequency taken to be a characteristic atomic vibrational frequency in the liquid. For a fixed $\mathbf{c}$, a plot of $\ln \tau_\alpha$ vs. T produces the well-known C-shaped time-temperature-transformation (TTT) diagram for the α-crystal nucleation. Below the α-liquidus temperature where the crystal becomes thermodynamically stable, competition between a rising W vs. a falling ΔG_α determines the TTT diagram. The TTT diagram exhibits a minimum crystallization time scale, τ^*_α, at an associated "nose" temperature, T^*_α , for which the nucleation time is minimized. One obtains τ^*_α and T^*_α by requiring $d\tau_\alpha/dT = 0$ at fixed $\mathbf{c}$. Assuming τ^*_α to be a well-behaved function of $\mathbf{c}$ and expanding τ^*_α vs. $\mathbf{c}$ in a Taylor series around an initial composition $\mathbf{c_o}$, one obtains the compositional dependence of τ^*_α for a small composition change, $\mathbf{c} - \mathbf{c_o}$, to leading order as

$$\tau^*_\alpha(\mathbf{c}) - \tau^*_\alpha(\mathbf{c_o}) \approx \exp[\boldsymbol{\lambda_\alpha} \cdot (\mathbf{c} - \mathbf{c_o})], \qquad [2]$$

where $\boldsymbol{\lambda_\alpha} = \nabla(\ln \tau^*_\alpha(\mathbf{c})) = \nabla[\{W(T^*, \mathbf{c}) + \Delta G_\alpha(T^*, \mathbf{c})\}/kT^*]$ is formally the gradient vector with respect to composition of $\ln \tau^*_\alpha(\mathbf{c})$ evaluated at a fixed composition, $\mathbf{c_o}$, and at the nose temperature T^*. Eq. **2** predicts that for the α-crystallization pathway, $\ln \tau^*_\alpha$ should vary exponentially with $\mathbf{c}$ for small compositional displacements, $\mathbf{c} - \mathbf{c_o}$. The exponential composition dependence is a consequence of crystal nucleation being a thermally activated process. The minimum crystallization time, τ^*_α, is a fundamental measure of GFA. According to the Fourier heat flow equation, one expects the time scale for cooling a molten sample to scale with the square of the lateral dimension of the sample, i.e., $\tau^*_\alpha \approx d^2_{cr}$. Accordingly, a GFA composition map that reflects the composition variation of τ^*_α can be constructed by mapping d^2_{cr} as a function of composition. This map would reflect the composition variation of τ^*_α for the α-crystallization event where such event has the shortest (i.e., the limiting) crystallization time. Collectively considering the set of all competing crystallization pathways for the various crystalline phases (e.g., α, β, γ, etc.), a global GFA composition map is constructed determined at each composition by the competing phase which has the shortest crystallization time. The overall GFA map will consist of piecewise

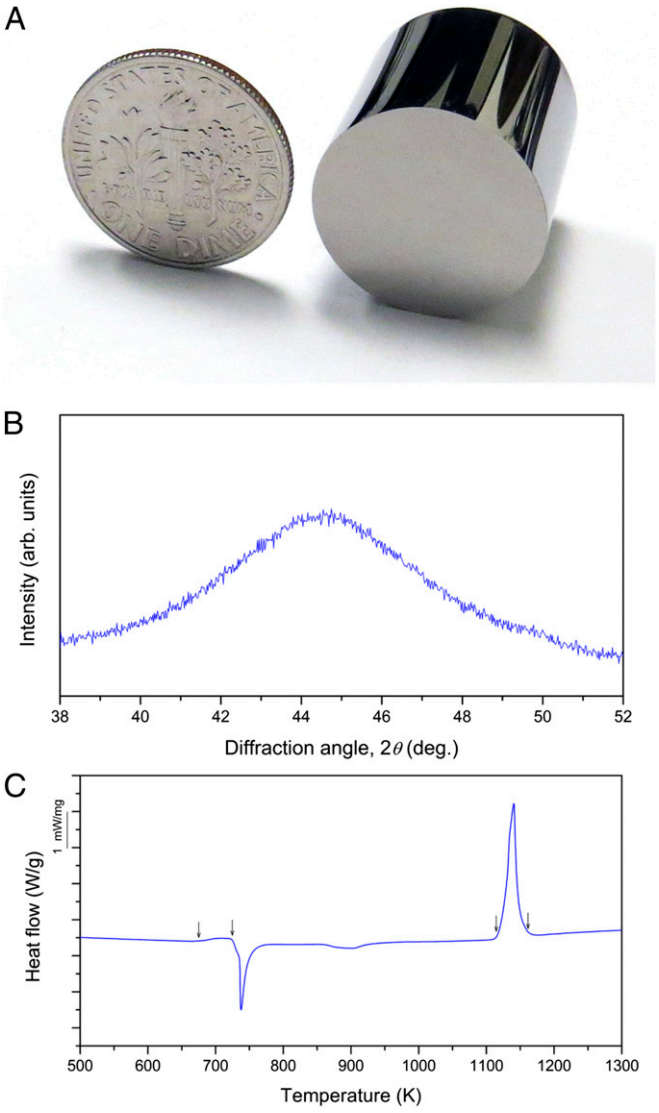

Fig. 3. (*A*) A sectioned 17-mm fully amorphous $Ni_{68.6}Cr_{8.7}Nb_3P_{16}B_{3.2}Si_{0.5}$ rod (section shown next to a dime for comparison). (*B*) X-ray diffractogram taken along the rod cross-section verifying the amorphous structure of the rod. (*C*) Differential calorimetry scan taken at 20 K/min scan rate. Arrows from left to right designate the glass transition, crystallization onset, solidus, and liquidus temperatures of 678 K, 722 K, 1119 K, and 1157 K, respectively.

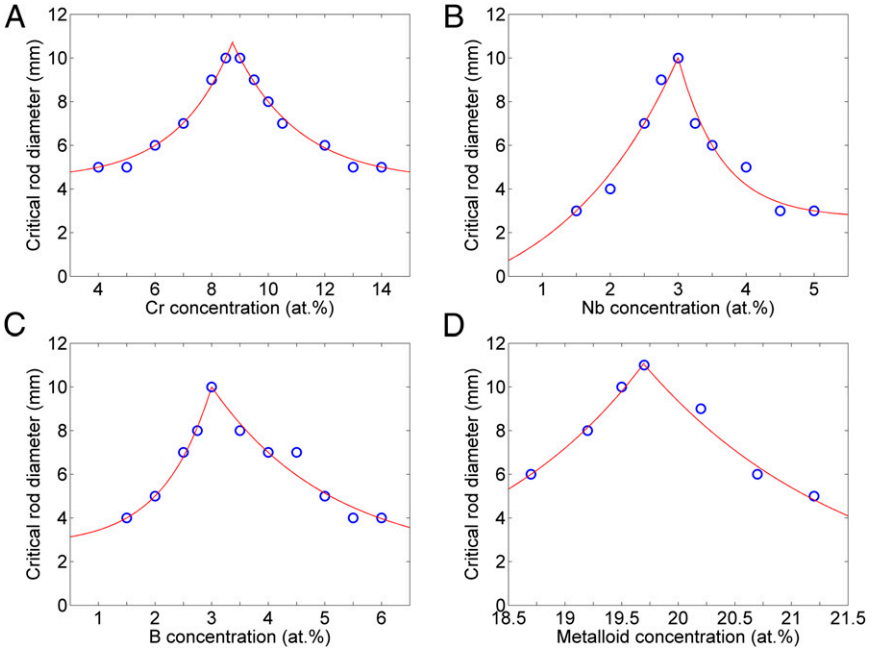

Fig. 4. Compositional dependence of GFA along four series intersecting a GFA peak at composition $Ni_{69}Cr_{8.5}Nb_3P_{16.5}B_3$. Solid lines are exponential fits to the experimental data (open circles) on each side of the peak. (*A*) Critical rod diameter d_{cr} plotted against the Cr atomic concentration as a substitute for Ni according to $Ni_{77.5-w}Cr_wNb_3P_{16.5}B_3$. (*B*) Critical rod diameter d_{cr} plotted against the Nb atomic concentration as a substitute for Cr according to $Ni_{69}Cr_{11.5-x}Nb_xP_{16.5}B_3$. (*C*) Critical rod diameter d_{cr} plotted against the B atomic concentration as a substitute for P according to $Ni_{69}Cr_{8.5}Nb_3P_{19.5-z}B_z$. (*D*) Critical rod diameter d_{cr} plotted against the atomic concentration of metalloids substituting for metals according to $(Ni_{0.8541}Cr_{0.1085}Nb_{0.0374})_{100-(y+z)}(P_{0.8376}B_{0.1624})_{(y+z)}$.

continuous exponential subsurfaces, indexed by α, β, γ, etc., which intersect to form exponential cusps at compositions associated with the cross-over in the nucleation pathway (e.g., from α to β, etc.).

According to Eq. **1**, GFA is determined by the competition of two thermally activated processes: that of forming the critical nucleus of the crystalline phase and that of configurationally rearranging the liquid, having respective activation barriers $W(T^*, \mathbf{c})$ and $\Delta G_\alpha(T^*, \mathbf{c})$. In our analysis, we only assume that these barriers are smooth functions of temperature and composition. The rising η with increasing undercooling can be well described by the liquid fragility parameter m, defined as $m = [d(\log\eta)/d(T_g/T)]_{T_g}$, together with the value of T_g (19). To lowest order, the driving force for crystallization with increasing liquid undercooling scales with $1 - T/T_L$, so that ΔG_α scales according to $(1 - T/T_L)^{-2}$ for modest undercooling (2). So at the Kauzmann temperature T_K where the entropy of the liquid is assumed to match the entropy of the crystal (also referred to as the ideal or thermodynamic glass transition) (20), the leading term in ΔG_α would be of order $(1 - T_K/T_L)^{-2}$. Here we assume that the calorimetric glass transition temperature T_g, which is readily accessible experimentally, adequately approximates T_K. As such, the leading term in ΔG_α is taken here to be of order $(1 - t_{rg})^{-2}$. Both t_{rg} and m are experimentally accessible material properties that provide a quantitative measure of the respective activation barriers along with their variation with composition. One can describe mathematically the dependence of the crystallization time scale τ_α^* on the independent parameters t_{rg} and m by examining the dependence of the activation barriers $W(T, \mathbf{c})$ and $\Delta G_\alpha(T, \mathbf{c})$ on these parameters (see *SI Materials and Methods* for a more detailed discussion). Below we argue that the observed compositional dependence of GFA in the present work is attributable almost entirely to the combined effects of varying t_{rg} and m with composition.

To clarify the origin of the composition dependence of GFA, we performed detailed calorimetric and rheometric measurements to evaluate both t_{rg} and m as functions of composition along the representative alloy series III (Fig. 4*C*), $Ni_{69}Cr_{8.5}Nb_3P_{19.5-z}B_z$ (see *Materials and Methods* for details on measurements of m and t_{rg}, and *SI Materials and Methods* for calorimetry and viscosity plots). A similar analysis can be applied to the other composition series. The GFA composition data along this series are plotted in terms of d_{cr}^2 vs. z in Fig. 5*A*; the data were fitted by two exponential functions of composition for the two branches of the GFA curve. For a local GFA maximum at composition $\mathbf{c_o}$, like the one at 3 atomic percent B (i.e., at $z_o = 3$), the τ_α^* values for two different competing crystallization pathways cross over and are mutually equal at z_o. We arbitrarily refer to the two crystal branches (low z and high z) of the GFA curve using crystal labels "α" and "β". Firstly, within the error of our calorimetry data, we observe that $\mathbf{c_o}$ is located quite precisely at a eutectic composition for which the alloy liquidus is minimum (see *SI Materials and Methods* for melting data). This is actually true for all of the alloy series I–IV (Fig. 4). GFA is therefore optimized very close to a quinary eutectic composition. The d_{cr} data for series I–IV, therefore, describe GFA along lines in composition space that all pass through this eutectic composition. From the calorimetric liquidus measurements along series III, the α region $z < z_o$ is a hypoeutectic (with a falling liquidus curve as z increases) region whereas the β region $z_o > z_o$ is hypereutectic (with a rising liquidus curve as z increases). Because t_{rg} depends inversely on the liquidus temperature, its composition dependence demonstrates a cusp-like maximum with discontinuous slope at z_o. The plot of t_{rg} along series III shown in Fig. 5*B* reveals this sharp discontinuity. Specifically, t_{rg} is highest at the eutectic composition and drops precipitously for $z > z_o$. In contrast, t_{rg} increases very slightly as z approaches z_o in the hypoeutectic region. On the other hand, the experimental liquid fragility, m, being a property of the liquid phase alone and independent of the crystal/liquid phase equilibria, is shown in Fig. 5*C* to be a continuous and monotonically decreasing function of $\mathbf{c}$. Specifically, m drops steeply as z increases with an approximately exponentially decaying trend. A decreasing m corresponds to a higher

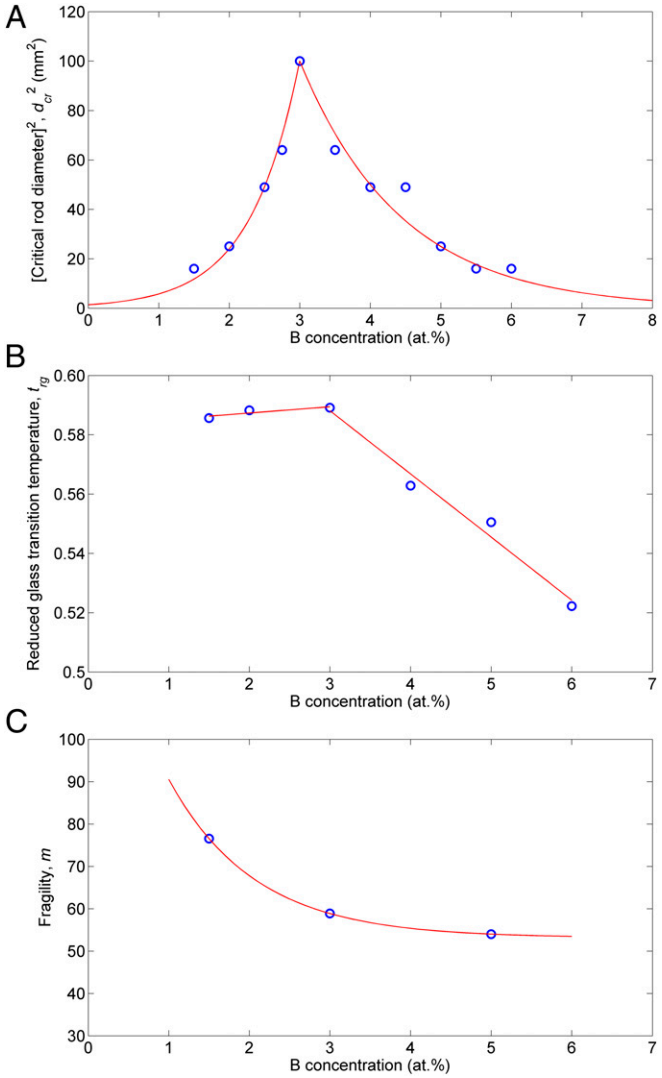

Fig. 5. (*A*) Compositional dependence of GFA plotted in terms of d_{cr}^2 against the B atomic concentration as a substitute for P according to $Ni_{69}Cr_{8.5}Nb_3P_{19.5-z}B_z$. Solid lines are exponential fits to the experimental data (open circles) on each side of the peak (at 3 at. % B). (*B*) Reduced glass transition temperature t_{rg} plotted against the B atomic concentration as a substitute for P according to $Ni_{69}Cr_{8.5}Nb_3P_{19.5-z}B_z$. Solid lines are polynomial fits to the experimental data (open circles) on each side of the cusp (at 3 at.% B). (*C*) Liquid fragility m plotted against the B atomic concentration as a substitute for P according to $Ni_{69}Cr_{8.5}Nb_3P_{19.5-z}B_z$. The solid line is an exponential fit to the experimental data (open circles).

viscosity throughout the undercooled liquid region, i.e., from T_g to T_L, thereby implying a greater viscosity at the nucleation temperature, T_α^*. One therefore expects GFA to increase with falling m.

By qualitatively analyzing the plots of Fig. 5 *B* and *C*, one can gain critical insight into the origin of the piecewise continuous form of the GFA function (Fig. 5*A*). The drop in t_{rg} for $z > z_o$ is steep and should lead to rapid exponential decay of GFA. This drop in t_{rg} in the hypereutectic β-region arises from a steep rise in T_L (*SI Materials and Methods*). In turn, this increases the crystallization driving force and steeply reduces ΔG_β such that GFA decays rapidly. For $z < z_o$, one has nearly constant or slightly rising t_{rg} as z increases. This slight rise in t_{rg} cannot explain the sharply rising GFA. Rather, the sharp GFA rise in the hypoeutectic α-region can be plausibly explained by the rapidly falling fragility, m. As the liquid structure becomes stronger (decreasing m with increasing B content), the rate at which atomic configurations are sampled at T_α^* slows, increasing the time to achieve a critical crystal nucleus, τ_α^*. The hypo- and hypereutectic branches of the GFA map are apparently the result of an interplay of the t_{rg} and m variations with composition.

To quantify the analysis above, consider Eq. **2** and the exponential decay parameters λ_α and λ_β obtained from the exponential fits to the GFA data for the respective hypo- and hypereutectic branches of the GFA curve. According to Eq. **2**, the discontinuity in the slope of $\ln d_{cr}^2$ vs. z at the GFA cusp is simply given by the difference $\lambda_\beta - \lambda_\alpha$. Without loss of generality, one can show that λ_α and λ_β can be separated into contributions arising from variations in t_{rg} and m, and potentially any other relevant material parameters that enter the expression for $\ln \tau_\alpha^*(\mathbf{c})$ (the mathematical details of this separation are presented in *SI Materials and Methods*). Using the chain rule to evaluate $\boldsymbol{\lambda_\alpha} = \nabla(\ln \tau_\alpha^*(\mathbf{c}))$, one obtains

$$\lambda_\alpha = \lambda_m - \lambda_{t_{rg,\alpha}} \quad \textbf{[3a]}$$

$$\lambda_\beta = \lambda_m - \lambda_{t_{rg,\beta}}. \quad \textbf{[3b]}$$

Here λ_m being a property of the liquid phase only, is identical for both branches; its composition dependence given by $\lambda_m = \{[d(\ln d_{cr}^2)/dm](dm/d\mathbf{c})\}_{t_{rg}}$. The $\lambda_{t_{rg}}$ parameters depend on the nucleating crystal and are different for α and β; they are given by $\lambda_{t_{rg}} = \{[d(\ln d_{cr}^2)/dt_{rg}](dt_{rg}/d\mathbf{c})\}_m$. The $\lambda_{t_{rg}}$ jumps discontinuously with varying $\mathbf{c}$ on going from the α- to the β-branch of the curve due to the change in the slope $dt_{rg}/d\mathbf{c}$ (as seen in Fig. 5*B*). It was already pointed out that the composition $\mathbf{c_o}$ of the GFA cusp coincides precisely with the eutectic composition (at which the α- and β-liquidus curves cross). From this, one can conclude that any other parameter that influences GFA (e.g., the melt–crystal interfacial energy for the α- and β-crystalline phases) must be nearly equal for both branches of the GFA curve. Were this not the case, the GFA cusp would be shifted off the eutectic composition, $\mathbf{c_o}$. The above facts suggest that λ_α and λ_β in Eqs. **3a** and **3b** are determined mainly by the measured composition dependences of t_{rg} and m. In this case, Eqs. **3a** and **3b** become a pair of linear equations with two unknowns, λ_m and $d(\ln d_{cr}^2)/dt_{rg}$. At the cusp composition, experimental fitting yields $\lambda_\alpha = 1.43$, $\lambda_\beta = -0.693$, $dt_{rg,\alpha}/d\mathbf{c} = 0.00211$, and $dt_{rg,\beta}/d\mathbf{c} = -0.0213$ (where $\mathbf{c}$ is in units of z, i.e., in atomic percentages of B, and d_{cr} is in millimeters; Fig. 5 *A* and *B* and *SI Materials and Methods*). Solving for the two unknowns one obtains $\lambda_m = 1.24$ and $d(\ln d_{cr}^2)/dt_{rg} = 90.6$, which give $\lambda_{t_{rg,\alpha}} = 0.191$ and $\lambda_{t_{rg,\beta}} = -1.93$. One finds that λ_α consists of a fragility contribution $\lambda_m/\lambda_\alpha = 87\%$, and a contribution from Turnbull's parameter $\lambda_{t_{rg,\alpha}}/\lambda_\alpha = 13\%$. In the hypoeutectic α-region, therefore, the decreasing liquid fragility parameter (i.e., the increasing liquid viscosity at the nucleation nose) dominates the exponential rise in GFA. By contrast, the negative λ_β consists of an overwhelming negative contribution from Turnbull's parameter $\lambda_{t_{rg,\beta}}/\lambda_\beta = 278\%$, and a positive contribution from fragility $\lambda_m/\lambda_\beta = -178\%$. Hence, the exponential GFA decay in the hypereutectic β-region would have been significantly greater (by a factor of 2.78) had the fragility of the liquid not been decreasing with increasing $\mathbf{c}$.

As follows from the analysis above, the Turnbull parameter and fragility alone give a plausible and self-consistent account of the composition variations of GFA. Specifically, the large variation in fragility over a fairly narrow compositional change has a dramatic effect on the compositional dependence of GFA; it steepens the GFA rise in the hypoeutectic region and offsets the GFA drop in the hypereutectic region. Finally, we note that from our fit for $m(z)$ in Fig. 5*C*, we have $dm/d\mathbf{c} = -5.4$ as evaluated at z_o. Using our value of λ_m, one obtains the intrinsic dependence of

GFA on m, i.e., $d(\ln d_{cr}^2)/dm = -0.23$. For a fixed t_{rg}, this value implies that a decrease in the fragility parameter m of about 4.5 is associated with a remarkable 65% increase in d_{cr}. Clearly, the liquid fragility m plays a very important role in determining glass formation. Mukherjee et al. (21) directly measured the TTT diagrams for a series of compositionally distinct Zr-based glasses all having nearly the same t_{rg} but varying liquid fragility. The measured τ_α^*, which was found to vary by more than 1 order of magnitude among these alloys, was shown to be directly proportional to the liquid viscosity at the nose temperature T_α^*. It was argued that the GFA variation among these Zr-based glasses arises mainly from the variation in fragility m. In a separate work, Na et al. (22) studied the fragility of compositionally distinct Fe-based metallic glasses, and showed that their GFA and fragility obey a fairly tight correlation that extended over nearly 2 orders of magnitude in τ_α^*. These studies are consistent with the key findings of the present work. One is naturally led to consider the numerous parameters and criteria proposed in the literature to guide the discovery of bulk metallic glasses (3, 6, 10–12, 21). Based on the present work, it is clear that the successful prediction of GFA requires, at a minimum, properly describing the roles of Turnbull's parameter and liquid fragility.

Materials and Methods

Alloy ingots were prepared by inductively melting pure elements in silica tubes under high-purity argon. The purity levels of the constituent elements were as follows: Ni 99.995%, Cr 99.996%, Nb 99.95%, P 99.9999%, B 99.5%, and Si 99.9999%. Amorphous rods were produced by remelting the alloy ingots in silica tubes having 0.5-mm-thick walls in a furnace at 1250 °C under high-purity argon, and after achieving a uniform temperature melt state, rapidly quenching in a stirred room temperature water bath. The 17-mm amorphous rod of $Ni_{68.6}Cr_{8.7}Nb_3P_{16}B_{3.2}Si_{0.5}$ was produced by remelting the alloy ingot together with dehydrated boron oxide flux in a silica tube having a 1-mm-thick wall in a furnace at 1350 °C under high-purity argon, and after allowing the melt to interact with the molten flux for ~2 h at 1350 °C, then rapidly quenching in a stirred room temperature water bath. To determine the GFA of each composition, two to four separate sample rods were produced with diameters varying in 1-mm increments. The reported values of d_{cr}, therefore, have an experimental uncertainly of ±0.5 mm. The amorphous structure of the rods was verified by X-ray diffraction using Cu$K\alpha$ radiation.

The reduced glass transition t_{rg} was evaluated by measuring the glass transition temperature, T_g, and the alloy liquidus temperature, T_L, and using differential scanning calorimetry. T_g was evaluated as the onset of the glass transition at a scan rate of 20 K/min. T_L was evaluated at a scan rate of 5 K/min to reduce scan rate effects and instrumental broadening of the melting transition.

The liquid fragility m was evaluated by measuring the temperature dependence of the equilibrium viscosity around the glass transition temperature. The equilibrium viscosity was measured by performing three-point beam bending of amorphous rods 2 mm in diameter and 10 mm in length using a thermomechanical analyzer, as described by Hagy (23) (*SI Materials and Methods*).

1. Turnbull D (1969) Under what conditions can a glass be formed. *Contemp Phys* 10(5): 473–488.
2. Spaepen F, Turnbull D (1984) Metallic glasses. *Annu Rev Phys Chem* 35:241–263.
3. Perepezko JH (1984) Nucleation in undercooled liquids. *Mater Sci Eng* 65(1):125–135.
4. Lin XH, Johnson WL, Rhim WK (1997) Effect of oxygen impurity on the crystallization of undercooled bulk glass forming Zr-Ti-Ni-Cu-Al alloy. *Mater T JIM* 38(5):473–477.
5. Kelton KF, Greer AL, Herlach DM, Holland-Moritz D (2004) The influence of order on the nucleation barrier. *MRS Bull* 29(12):940–944.
6. Gangopadhyha AK, Hyers RW, Kelton KF (2012) Nucleation and thermophysical properties of glass forming liquids. *J Met* 64(9):1109–1117.
7. Lohwongwatana B, Schroers J, Johnson WL (2006) Strain rate induced crystallization in bulk metallic glass-forming liquid. *Phys Rev Lett* 96(7):075503.
8. Chen HS, Turnbull D (1970) Formation and stability of amorphous alloys of Au-Ge-Si. *Acta Metall* 18(2):261–263.
9. Chen HS, Turnbull D (1968) Evidence of a glass transition in a gold-germanium-silicon alloy. *J Chem Phys* 48(6):2560–2571.
10. Inoue A (2000) Stabilization of metallic supercooled liquid and bulk amorphous alloys. *Acta Mater* 48(1):279–306.
11. Johnson WL (1999) Bulk glass-forming metallic alloys; science and technology. *MRS Bull* 24(10):42–56.
12. Lu ZP, Liu CT (2003) Glass formation criterion for various glass-forming systems. *Phys Rev Lett* 91(11):115505.
13. Habazaki H, et al. (1989) The anodic behavior of amorphous Ni-19P alloys in different amorphous states. *Corros Sci* 29(11-12):1319–1328.
14. Zhang B-P, Habazaki H, Kawashima A, Asami K, Hashimoto K (1992) The corrosion behavior of amorphous Ni-Cr-P alloys in concentrated hydrofluoric acid. *Corros Sci* 33(10):1519–1528.
15. Habazaki H, Ukai H, Izumiya K, Hashimoto K (2001) Corrosion behavior of amorphous Ni-Cr-Nb-P-B bulk alloys in 6M HCl solution. *Mater Sci Eng A* 318(1-2):77–86.
16. Wang X, Yoshii I, Inoue A, Kim Y-H, Kim I-B (1999) Bulk amorphous $Ni_{75-x}Nb_5M_xP_{20-y}B_y$ (M=Cr, Mo) alloys with large supercooling and high strength. *Mater T JIM* 40(10): 1130–1136.
17. Demetriou MD, et al. (2006) Cooperative shear model for the rheology of glass-forming metallic liquids. *Phys Rev Lett* 97(6):065502.
18. Johnson WL, Demetriou MD, Harmon JS, Lind ML, Samwer K (2007) Rheology and ultrasonic properties of metallic glass forming liquids: A potential energy landscape perspective. *MRS Bull* 32(1-2):644–650.
19. Angell CA (1995) Formation of glasses from liquids and biopolymers. *Science* 267(5206):1924–1935.
20. Kauzmann W (1948) The nature of the glassy state and the behavior of liquids at low temperatures. *Chem Rev* 43(2):219–256.
21. Mukherjee S, Schroers J, Johnson WL, Rhim WK (2005) Influence of kinetic and thermodynamic factors on the glass forming ability of Zr-based bulk amorphous alloys. *Phys Rev Lett* 94(24):245501.
22. Na JH, Demetriou MD, Johnson WL (2011) Fragility of iron-based glasses. *Appl Phys Lett* 99(16):161902.
23. Hagy HE (1963) Experimental evaluation of beam bending method of determining glass viscosities in the range 10^8 to 10^{15} Poise. *J Am Ceram Soc* 46(2):93–97.